

Article

Bubble Dynamics in a Narrow Gap Flow under the Influence of Pressure Gradient and Shear Flow

Peter Reinke ^{*}, Jan Ahlrichs, Tom Beckmann  and Marcus Schmidt 

Department of Fluidmechanics, HAWK University of Applied Sciences and Arts Goettingen, Faculty I, 37085 Goettingen, Germany; jan.ahlrichs@hawk.de (J.A.); tom.beckmann@hawk.de (T.B.); marcus.schmidt@hawk.de (M.S.)

* Correspondence: peter.reinke@hawk.de; Tel.: +49-551-3705-264

Received: 17 October 2020; Accepted: 12 November 2020; Published: 16 November 2020



Abstract: The volume-of-flow method combined with the Rayleigh–Plesset equation is well established for the computation of cavitation, i.e., the generation and transportation of vapor bubbles inside a liquid flow resulting in cloud, sheet or streamline cavitation. There are, however, limitations, if this method is applied to a restricted flow between two adjacent walls and the bubbles' size is of the same magnitude as that of the clearance between the walls. This work presents experimental and numerical results of the bubble generation and its transportation in a Couette-type flow under the influence of shear and a strong pressure gradient which are typical for journal bearings or hydraulic seals. Under the impact of variations of the film thickness, the VoF method produces reliable results if bubble diameters are less than half the clearance between the walls. For larger bubbles, the wall contact becomes significant and the bubbles adopt an elliptical shape forced by the shear flow and under the influence of a strong pressure gradient. Moreover, transient changes in the pressure result in transient cavitation, which is captured by high-speed imaging providing material to evaluate transient, three-dimensional computations of a two-phase flow.

Keywords: cavitation; Couette flow; bubble dynamics; small clearance; computed flow dynamics; experiment

1. Introduction

The research of bubble dynamics has a general relevance for numerous technical applications where a hydrodynamic gap is the core element that either carries the load (journal bearing) or separates machine compartments (hydraulic seal). In both cases, the fluid film is subject to a shear flow due the differential velocity of the adjacent walls and a significant pressure gradient. Under transient operational conditions, the pressure gradient varies over time, combined with a change in fluid film thickness regions with low local pressure can occur that can result in cavitation, if the local pressure falls below a critical value.

At this point, the concept of cavitation must be briefly discussed. Firstly, we must ask, where is the cavity formed? Secondly, what is the fluid and what matter fills the bubble? Thirdly, we will address a selection of mechanisms that cause cavitation in journal flows. There are numerous works that have researched cavitation. Borbe's dissertation [1] is a fundamental work on flow cavitation and a review for journal bearings is given by Braun and Hannon [2]. In summary, both works suggest a general differentiation of cavitation into three sub-sections, which are laid out in Table 1 below. It is confirmed that only vapor cavitation may result in material cavitation due to the extremely short condensation time. For the generation of voids, Sun and Brewe [3] computed a time of 0.167 ms for the case of vapor cavitation whereas they found values of 3×10^5 s for gaseous cavitation. Consequently, one would assume that only vapor cavitation is an issue for typical small gap flows where the residual time of

the fluid inside the critical zone is significantly less than 1 s. However, a recent study of Pendowski and Pischinger [4] strongly suggested that under transient conditions, the application of the otherwise reliable Henry’s law is not valid and substantially shorter formation times of gas voids have to be applied, which are closer to the order of magnitude of evaporation.

Table 1. Cavitation. Definition of expressions according to [1,2].

Type	Fluid Cavitation		Material Cavitation
location of cavity	void in the liquid formed by gaseous matter		cavity in the wall caused by repetitive implosions of vapor bubbles
Type	Gaseous Cavitation	Pseudo Cavitation	Vapor Cavitation
matter filling the bubble	released gas (pure)	mixture of released gas and evaporated liquid	evaporated liquid (pure vapor)
fluid	liquid containing dissolved gas	liquid containing dissolved gas	pure liquid

This paper focusses on vapor cavitation, i.e., the formation of voids inside the liquid, their growth and transportation inside the fluid film. Xu et al. [5] describe the dynamics of bubbles in relation to the clearance between adjacent walls and explain that the structural change of the bubble dynamics is related to the coalescence of the bubbles. They define a wide gap if the clearance is greater than 0.3 mm and small gaps, if the clearance is less than 0.3 mm. Consequently, this study deals with a small gap flow, because the clearance in the critical section of the fluid film is 0.15–0.3 mm.

Tryggvason et al. [6] point out that it is important to consider the multi-scale aspect of small gap flows, because it makes the application of otherwise well established numerical methods difficult due to the aspect ratio of film thickness vs. width and length scale. However, the correct prediction of vapor formation in liquid films requires a transient and three-dimensional model, which is documented in studies by Braun and Dzodzo [7] and Schmidt [8]. Experimental results of Nobis [9] confirm the numerical data given by [8].

One reason for the technical relevance of research stems from the fact that hydrodynamic journal bearings, which are a major component for internal combustion engines due to their simple design, are subject to cavitation, which might result in a potential breakdown of the engine itself. It might be assumed that pure vapor cavitation is merely a theoretical case due to the aeration of the lubricant under normal operation conditions [4]. However, this work deals with vapor cavitation, because of the documented cases of material cavitation that are listed below and because of the extremely short time scales that are reported in the results section of this work. Reviews pertaining to cavitation in journal bearings are given by Gläser [10] and [2] as well as summarized by ISO 7146 [11]. Based on [10], Garner et al. [12] and Engel [13] Table 2 describes four types of cavitation and their relation to particular features, which are characteristic for journal bearings in internal combustion engines.

Table 2. Forms of cavitation characteristically for journal bearings [10,12,13].

Type	Flow Cavitation	Impact Cavitation	Suction Cavitation	Exit Cavitation
transient condition	local flow velocity	rotating shaft boring	rapid shaft displacement	rapid shaft displacement
bearing structure	grooves feed holes	shaft boring	-	groove

All of these types of cavitation require a transient condition. Hence, it is necessary that experiments must include means to change the conditions of the fluid film either geometrically (film thickness)

or physically (flow rate) and numerical models must be transient and the meshing must adapt to a variable film thickness. Moreover, the numerical model has to be three-dimensional, which is substantiated by the results of Almqvist and Larson [14] as well as [8], who describe the limitations of a two-dimensional model applied to a fluid film flow. Sharma et al. [15] point to the difficulties in describing the phase boundary when the two-phase flow becomes more complex than a bubbly flow. In summary, a transient and three-dimensional dimensional flow, which is subject to cavitation, requires more research to understand the generation of voids inside the liquid and its transportation.

2. Experimental Apparatus and Set-Up

The experimental set-up is a Couette flow apparatus where a cylinder (1) is located inside a housing with a cylindrical cavity (2). The cylinder rotates with a given rotational speed ω_1 and is positioned eccentrically in relation to the axis of the cavity. Due to the rotation of the cylinder, a journal bearing type flow develops inside the fluid film. The cavity encloses the cylinder completely thus, the clearance at top and bottom of the cylinder give space for a cross flow, from the pressure maximum towards the pressure minimum which are caused by the circumferential flow, creating a three-dimensional flow structure. Figure 1 displays the design features of the experiment.

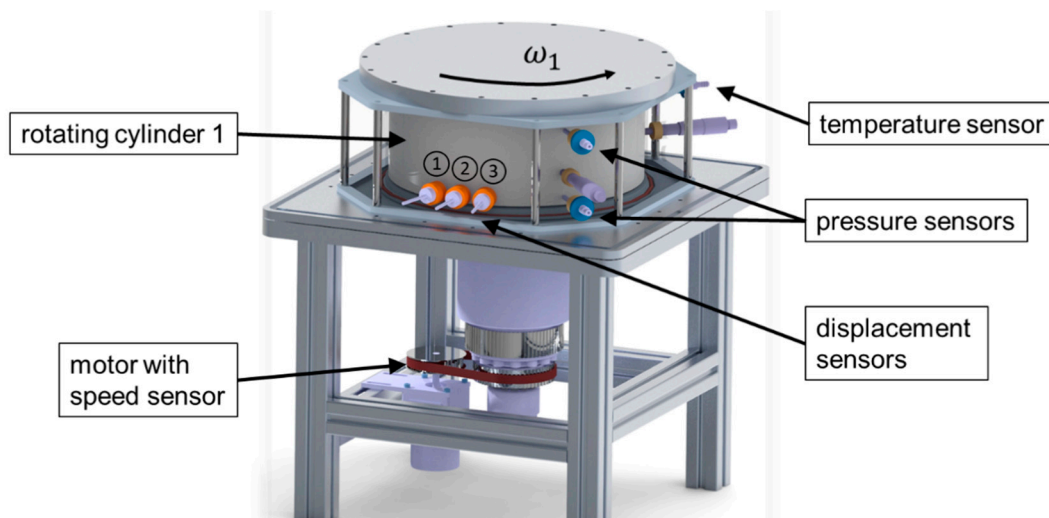


Figure 1. Experiment, Couette apparatus consisting of cylinder (1) rotating in a transparent cavity (2), combined with motor and sensors.

Figure 2 indicates the main parameters of the experiment and Couette flow. A cylinder (1) with its center M_1 rotates inside a cylindrical cavity (2) with its center M_2 that is also the origin of the coordinate system. The position (1') indicates a virtual alignment which represents an ideally rigid system whereas, the real system is elastic and the pressure building in the converging gap pushes the inner cylinder sideways into position (1). The momentary displacement of the inner cylinder in relation to the origin is

$$\vec{e}_1 = \begin{pmatrix} \Delta x_1 \\ \Delta y_1 \end{pmatrix}, \tag{1}$$

which is equal to the momentary eccentricity and a function of the rotational angle. The time derivative of the rotational angle is the rotational speed of cylinder (1)

$$\omega_1 = \frac{d\phi}{dt}. \tag{2}$$

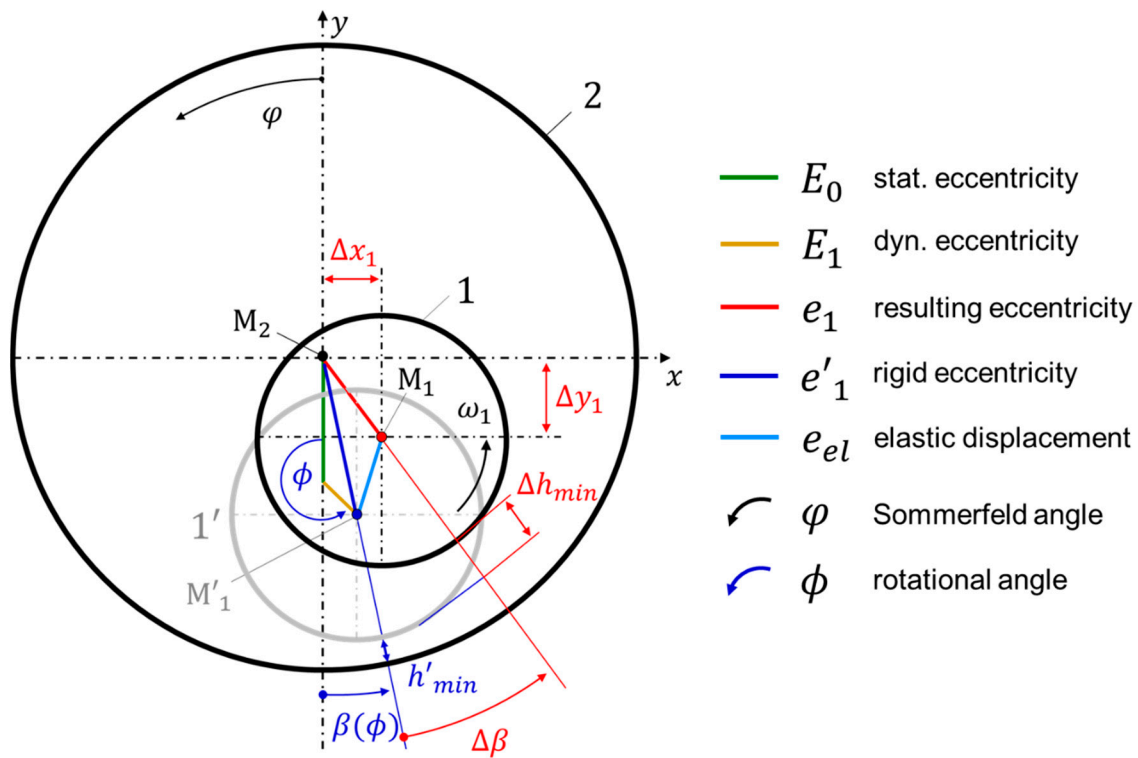


Figure 2. Main parameters of experiment and Couette flow.

Moreover, the static eccentricity E_0 denotes the distance between M_2 and the axial centerline of the shaft, which supports cylinder (1), and the co-axial alignment of (1) against the centerline is given by the dynamic eccentricity E_1 . Similar to the well known crankshaft kinematics Equation (3) describes the transient function for the momentary film thickness under rigid conditions.

$$h'_{min} = H_0 - E_0 \cdot \sqrt{1 + \lambda^2 - 2 \lambda \cos \phi}, \tag{3}$$

which is equal to the corrected reading of the displacement sensors

$$h'_{min} = H_{min} + E_1 \cos \phi. \tag{4}$$

The angular position of the minimum film thickness h_{min} oscillates with

$$\arctan \beta(\phi) = -\lambda \sin \phi. \tag{5}$$

When the system is operated with the speed ω_1 a pressure is building inside the converging gap and the system is subject to an elastic displacement e_{el} that is resulting in Δh_{min} and $\Delta \beta$, which are indicated in Figure 2 and are both, detected by the displacement sensors.

Including the elastic displacement of the rotating cylinder (1) the momentary minimum film thickness is defined by

$$h_{min} = h'_{min} + \Delta h_{min}. \tag{6}$$

3. Measurement Equipment

The flow and the fluid condition are monitored by displacement, pressure and temperature sensors, which are indicated in Figure 1. Additionally, rotational speed and motor torque are measured.

3.1. Fluid Film Thickness

The location of the minimum clearance is fundamentally important to understand the eccentric Couette flow and according to the Reynolds equation, the magnitude of the eccentricity defines the location and magnitude of the pressure gradient. Moreover, magnitude and orientation of the eccentricity define the angular position of the pressure extrema. Thus, the clearance between cylinder and cavity is monitored by means of three displacement sensors, whilst the middle sensor (2) located at a Sommerfeld angle φ of 180° and the neighbor sensors arranged symmetrically at a lateral distance δ , respectively. By applying a second-order interpolation, the three individual displacement values y_i and their corresponding lateral positions yield the magnitude of h_{min}

$$h_{min} = y_2 + \frac{k}{4} \tag{7}$$

and the lateral position

$$\beta = k \delta \tag{8}$$

with

$$k = \frac{y_3 - y_2}{2(y_1 + y_3 - 2y_2)} \text{ and } \delta = 11^\circ. \tag{9}$$

3.2. Camera

A high-speed camera (Dantec Phantom Miro 110) is used to capture bubble formation and transport inside the liquid film. The throughput of the camera is limited to 1.6 Gpx/s. Hence, resolution and frame rate have to be balanced. The experiment is recorded with a resolution of 640×480 pixels at 5400 fps. Based on a physical resolution of 80 px, which defines the minimum detection limit for the smallest bubble, the maximum exposure time is set at 100 μ s. Additionally, major equipment includes a large aperture macro lens (Tokina AT-X M100 Pro D Macro) and artificial lighting (2 LED spotlights Hedler ProfiLux LED 1000 á 25,000 lm) that is completing the set-up. Due to the experiment's physical dimensions, the lens has to support close focus with a respective magnification ratio of 1:1.

Figure 3 shows the camera's view and two image areas are indicated, which are used to show photographic and visualized numerical results in Section 8 of this paper. The image areas are downstream of the absolute minimum film thickness H_{min} inside the divergent section of the fluid film. The Sommerfeld angle φ marks the lateral position. A precision machined and polished housing made of acrylic (PMMA) provides the best optical quality and the octagonal outer shape enables an unrestricted radial optical access into the cavity. The camera is aligned perpendicular to the octagon's side, which is adjacent to the Sommerfeld angle of 180° in order to achieve optimum image quality in the region of the divergent cross-section of the fluid film.

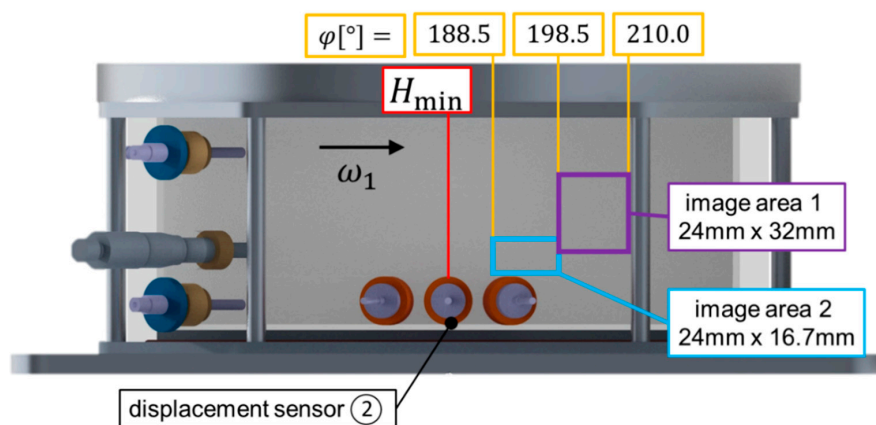


Figure 3. Optical access into the fluid film, viewing area located downstream of minimum film thickness.

4. Analogy and Fluid Design

The diagram displayed in Figure 4 puts this work into a broader perspective in relation to other studies pertaining to the Taylor-Couette flow at low clearance ratios. The diagram shows the Reynolds number and the clearance ratio that are addressed in this work. It can be surmised that the flow is of a laminar nature due to the distance to the stability limit proposed by DiPrima [16] and the occurrence of Taylor vortices is not that expected if compared to the results by Eagles et al. [17]. Moreover, Kahlert [18] investigated in his dissertation the validity of computing the lubrication flow without convective terms and proposed the limit

$$Re \cdot \Psi = 1 \tag{10}$$

when convective terms can be neglected. The flow, which is subject to the work on hand, marks the corner of a parameter range that is subject to future research, which extends towards the operational range of journal bearings for instance in CI-engines. This connection to technical applications founds on a similarity analysis and resulting in the Couette apparatus which is an experimental model derived from the lubricant flow in journal bearings. In a previous work, the authors [19] have proposed a similarity approach to compare the flow of the model experiment with a real bearing. The procedure shall be briefly outlined here. The main similarity numbers are: normalized clearance Ψ , Reynolds number Re and a kinematic parameter K which are derived from the actual geometry and operational parameters listed in Table 3 as well as physical restrictions such as the camera performance given by its resolution and frame rate. The kinematic parameter is defined by the dynamic changes in eccentricity related to suction cavitation, in particular [19]. Thus, the first anchor in the operational chart displayed in Figure 5 is the time scale, which in turn leads to the requirements of the fluid when geometrical scale and Re are taken into consideration. Hence, the point of operation is fixed based on the fluid's properties and the operational conditions, i.e., rotational speed, fluid temperature, static pressure inside the cavity. Future work will then include dynamic tests carried out varying the eccentricity's magnitude and change rate.

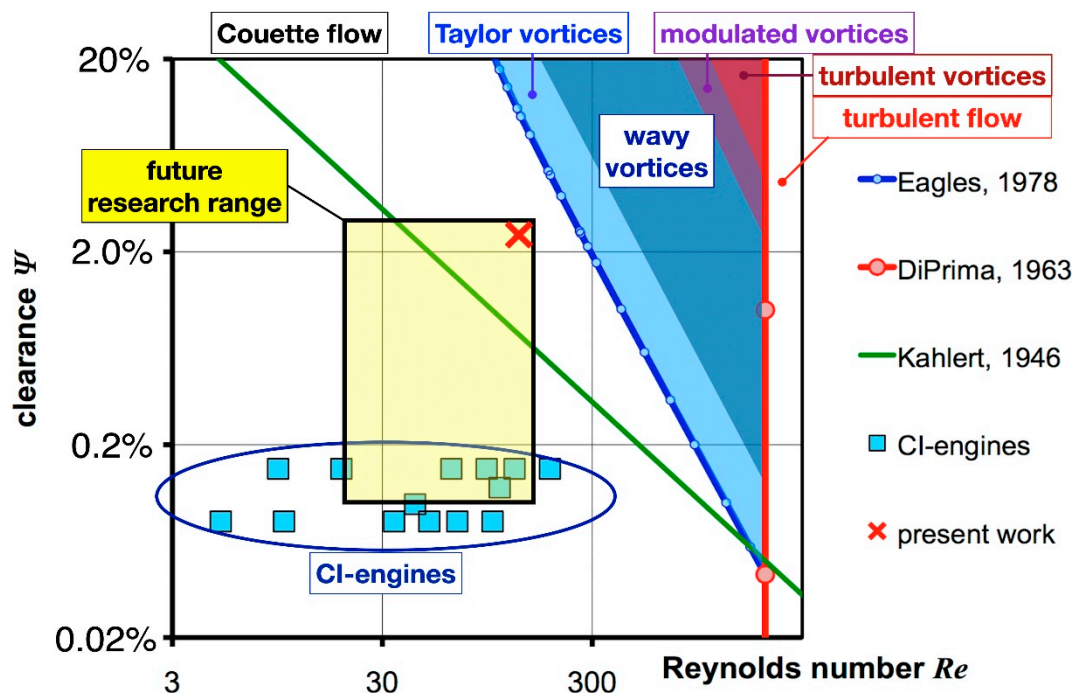


Figure 4. Stability diagram of the Taylor-Couette flow derived from Reinke et al. [19].

Table 3. General parameters of experiment and the narrow gap flow related to Figure 2.

Symbol	Value	Definition	Description
B	111.0 mm		cylinder height
E_0	3.417 mm		static eccentricity
E_1	0.030 mm		dynamic eccentricity
H_0	3.62 mm	$R_2 - R_1$	clearance, average fluid film thickness
H_{min}	0.173 mm	$R_2 - R_1 - E_0 - E_1$	minimum fluid film thickness
R_1	146.44 mm		cylinder radius
R_2	150.06 mm		cavity inside radius
ϵ_0	94.4%	$\frac{E_0}{H_0}$	normalized static eccentricity
ϵ_1	0.829%	$\frac{E_1}{H_0}$	normalized dynamic eccentricity
λ	0.878%	$\frac{E_1}{E_0}$	eccentricity ratio
Ψ	2.47%	$\frac{E_0^D}{H_0}$	normalized clearance
ω_1	23.2 1/s		angular frequency
Re	134	$\frac{\omega_1 R_1^2 \Psi \rho_0}{\mu_0}$	Reynolds number

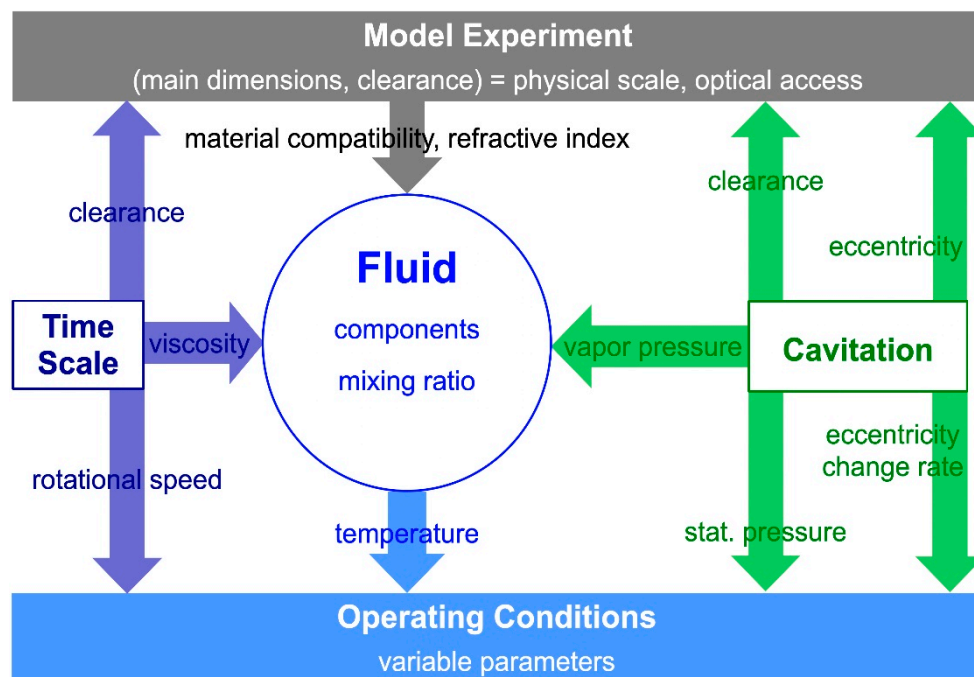


Figure 5. Operational chart and relations between the main similarity numbers and physical parameters.

The core component of the experiment is the fluid, which must be selected properly, because its viscosity defines Re and time scale. Moreover, the pressure distribution is directly depending on the viscosity and together with the fluid’s vapor pressure defining the boiling point or in other words the operational point of cavitation.

For this purpose, the authors [20] have developed a special cavitating fluid, which was already applied successfully to demonstrate that a cavitating Taylor-Couette flow shows a double transition: Taylor vortices and vaporization simultaneously at one operation point. The fluid in question is a mixture of a low boiling pentane, which triggers cavitation, and a long chain alkane (paraffin) to meet viscosity and refractive index. The fluid has been tested to be chemically compatible with all components of the model experiment. The relation between pressure and other restricting parameters defines the target value for the vapor pressure of the fluid that must show cavitation under the operation conditions of the model experiment. Moreover, the fluid must have an appropriate viscosity and refractive index, which is compatible with the housing material of the model experiment, enabling

the application of optical measurement of fluid velocity, bubble size and visualization. A detailed description of the fluid design can be found in [21] and the thermodynamic properties of the cavitating fluid are listed in Table 4. The value of the bulk modulus is adopted from data given by Watter [22] for mineral oil, because the cavitating fluid uses alkenes as basic liquid.

Table 4. Thermodynamic properties of the cavitating fluid at $T = 20\text{ }^\circ\text{C}$.

Symbol	Value	Description
ρ_0	868 kg/m ³	density
μ_0	80 mPa s	dynamic viscosity
K_0	1.5×10^9 Pa	bulk modulus

5. Numerical Model

The numerical model must be tailored to the particular conditions given by the small gap. The domain is not isometric, because the film thickness, the radial dimension is more than two orders of magnitude smaller than axial and angular dimension. One of us (M.S.) has developed a numerical model that fulfills the necessary requirements [8,23].

The first step is the meshing of the fluid domain and pertaining to computing efficiency and robustness, a block-structured mesh has been supplied most successfully. The schematic of the computational domain of the numerical simulation is shown in Figure 6. The grid for the fluid film between cylinder and cavity surface is created with the blockMesh tool included in the open source data bank [24]. The grid is generated as a block-structured mesh with wall-adapted cells to increase the numerical accuracy and to keeping the computing time acceptable. A recent joint research project carried out by [25] confirmed that a minimum number of cells must be applied to the fluid film in the radial direction. By means of a sensitivity test (Figure 7) based on deviations of velocity profiles at two lateral positions inside the fluid film (Figure 8) it is determined that 12 cells applied achieve the acceptable radial resolution for the expected Reynolds number range. Moreover, not only is the radial number of cells important for optimized efficiency and convergence but the aspect ratio must be applicable and based on Kistner’s recommendation [26]. Hence, the range of the aspect ratio is 4.2–6.5 for the work on hand.

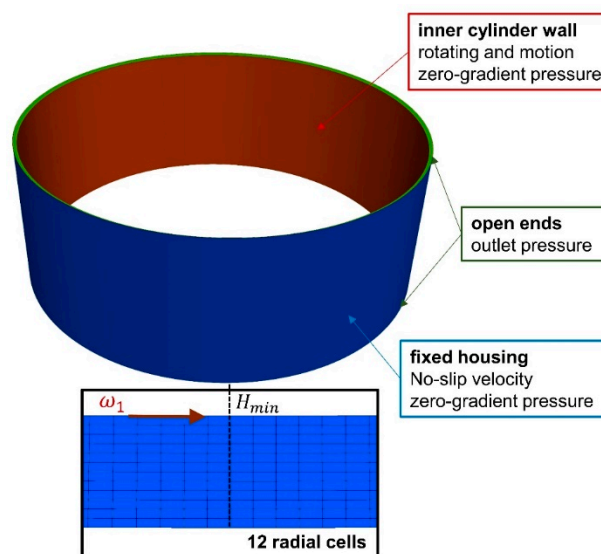


Figure 6. Meshing of the region in the vicinity of the minimum film thickness.

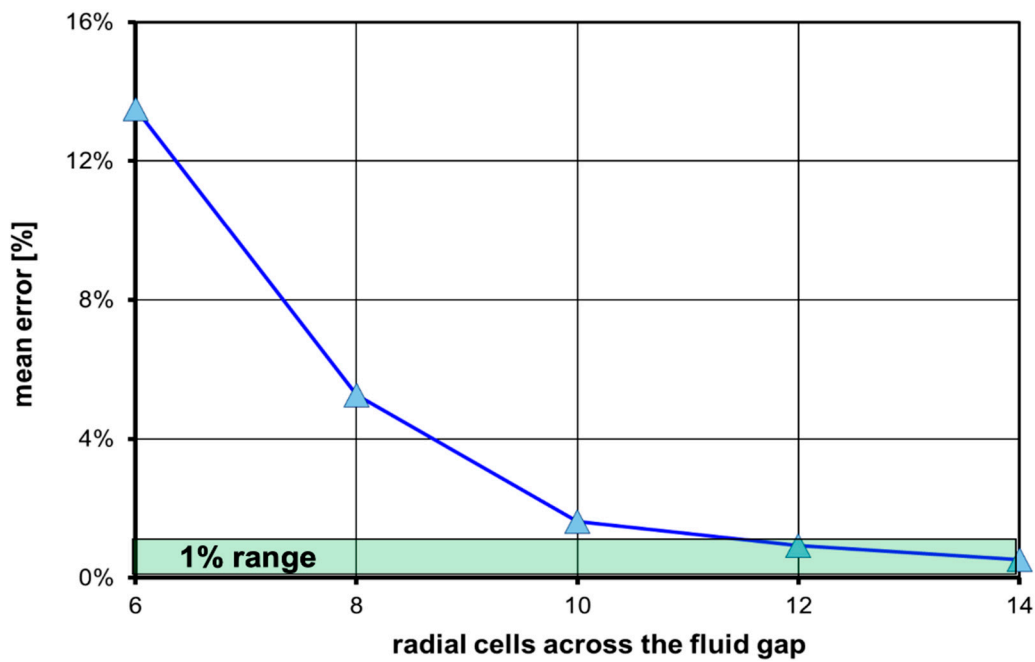


Figure 7. Results of sensitivity test, necessary number of radial cells for $Re = 40$ and $\varepsilon = 0.95$.

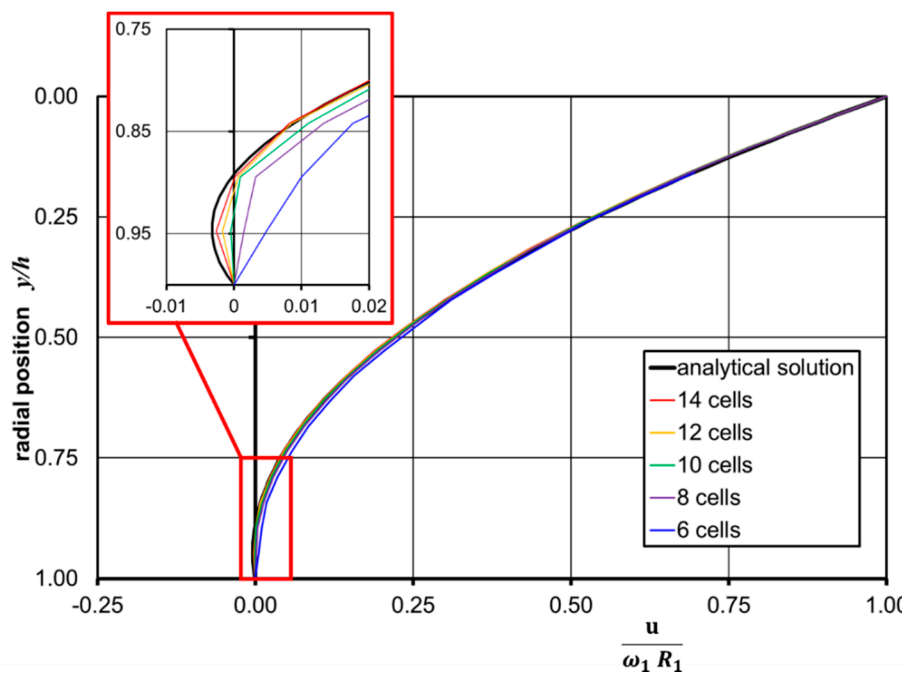


Figure 8. Radial velocity profiles at $\varphi = 200^\circ$ (left) for a 1D Sommerfeld flow with $Re = 40$ and $\varepsilon = 0.95$.

The simulation model and the boundary conditions are shown in Figure 6. The domain of the fluid film has three boundaries. The housing is fixed and its surface boundary is defined with a no-slip condition for the velocity and a zero gradient condition for the pressure. The rotating inner cylinder has a surface velocity, which is defined by the motion vector incorporating a combination of the surface rotational velocity and the displacement velocity. Finally, a boundary condition was implemented at the bottom and the top end of the fluid film enabling a cross flow from high to low pressure in the circumferential gap flow. The result is an outflow and inflow of the fluid and its magnitude depends

on the pressure difference. Additionally, the reference pressure related to the experiment is defined at both ends.

Another important feature of the meshing is a micro flexibility, which is needed to incorporate the relative movement of the rotating cylinder, which results in a cyclic variation of the magnitude and the angular position of the minimum film thickness. This feature of the mesh is realized by the dynamic mesh functionality of the of the open source code combined with an implemented boundary condition for the wall motion of the inner cylinder. For each time step, the displacement of the center of the rotating cylinder (1) is included according to Equation (1) based on measured data from the experiment. The transformation of the measured values into functional data is outlined in Section 3.1. The motion of the mesh structure is characterized by stretching and squeezing of the volume cells within the fluid film, which results in a true simulation of the local change in film thickness that is unique for the suction type cavitation. In the following, the positional change of the grid points is calculated on the basis of a Laplace equation. To avoid a local deterioration of the mesh quality, the deformation and distortion of the grid points are distributed uniformly over the solution domain, as explored by Jasak et al. [27].

The simulation of the complex and three-dimensional two-phase flow was performed by using the software OpenFOAM, which is based on the finite volume method and utilizes a mass balance equation and the three-dimensional, incompressible Navier–Stokes equations in detail described by Ferziger and Perić [28]. Equation (12) is expanded by a surface tension term and the time-varying field forces. The two-phase flow requires an additional transport equation for the liquid volume fraction α , which is normalized by the total volume of liquid and gas phase. All equations require transient time-dependent solvers. The Equations (11)–(13) are discretized in space and time using second-order accuracy methods. The initial time step size is 10^{-6} and is adjusted during the calculation to fulfill the Courant–Friedrichs–Lewy (CFL) condition by keeping the CFL value below unity. The relevant equations are the following:

The continuity equation

$$\frac{\partial \rho}{\partial t} + \vec{\nabla} \cdot (\rho \vec{u}) = 0, \tag{11}$$

an extended Navier-Stokes equation

$$\frac{\partial \rho \vec{u}}{\partial t} + \rho(\vec{u} \cdot \vec{\nabla}) \vec{u} = \rho \vec{g} - \sigma \frac{1}{R} \vec{n} - \vec{\nabla} p + \mu \vec{\nabla} \cdot (\vec{\nabla} \vec{u}) \tag{12}$$

and additionally, the transport equation for the liquid volume fraction according to Sauer [29]

$$\frac{\partial \alpha}{\partial t} + \vec{\nabla} \cdot (\alpha \vec{u}) + \vec{\nabla} \cdot [\alpha (1 - \alpha) \vec{u}_\alpha] = \frac{\dot{m}^+ + \dot{m}^-}{\rho}, \tag{13}$$

which calls for the definition of the liquid volume fraction

$$\alpha = \frac{V_l}{V_l + V_v}. \tag{14}$$

The computation of the two phase flow is based on the Schnerr–Sauer model [30], which applies the Rayleigh equation

$$\dot{R}_B = \sqrt{\frac{2}{3} \frac{|p_v - p(\phi)|}{\rho}}. \tag{15}$$

Recently, Kumar et al. [31] published a benchmark study that discussed the configuration of the vapor model for the application on the flow inside a nozzle. The Schnerr–Sauer model includes two empirical parameters C_V and C_C describing the mass flow at evaporation \dot{m}^+ and condensation \dot{m}^- at

the source term on the right side of Equation (13), respectively. The mass flow rates are described as follows, for evaporation

$$\dot{m}^+ = 3 \operatorname{sgn}[p_v - p(\phi)] \cdot \frac{\rho_l \rho_v \dot{R}_B}{\rho R_B} \cdot \alpha (1 - \alpha) \cdot C_V \quad (16)$$

and for condensation

$$\dot{m}^- = 3 \operatorname{sgn}[p_v - p(\phi)] \cdot \frac{\rho_l \rho_v \dot{R}_B}{\rho R_B} \cdot \alpha (1 - \alpha) \cdot C_C. \quad (17)$$

An additional parameter of the Schnerr–Sauer model is the bubble number density per unit volume and according to [29], it is originally recommended to be $10^{13}/\text{m}^3$. In an earlier project, the authors [32] investigated the impact of the bubble number density on the numerical result by means of a DoE for the simulation of an eccentric Couette flow. However, the model described in the work on hand makes use of a bubble number density of $10^{13}/\text{m}^3$ and the initial nuclei radius is $2 \mu\text{m}$. This ensures that there is at least one nuclei in each volume cell of the model.

Another aspect which [31] included in their work compares the validity of the Schnerr–Sauer model vs. the Zwart–Gerber–Belrami model. The results show that for a compressible flow, the Zwart–Gerber–Belrami model is more accurate for turbulent flows at high Reynolds numbers. However, taking the properties of the cavitating fluid (Table 4) into account, the compressibility can be calculated based on a simplified Tait equation which was suggested by [31]

$$\left(\frac{\rho}{\rho_0}\right)^\kappa = \frac{K_0 + \kappa \Delta p}{K_0} \quad (18)$$

which is developed in a Taylor progression of first order resulting in

$$\frac{\rho}{\rho_0} = 1 + \frac{\Delta p}{K_0} \quad (19)$$

and with

$$\Delta p = p_{\max} - p_0 = 127 \text{ kPa} \quad (20)$$

Equation (19) yields

$$\frac{\rho}{\rho_0} = 1.000085. \quad (21)$$

In other words, it can be surmised that compressibility can be neglected under the given conditions.

6. Elasticity

The pressure gradient, which is the driving factor of the bubble development, has its maximum in the vicinity of the minimum film thickness and its magnitude is strongly affected by the eccentricity. Therefore, it is important to measure the displacement of the rotating cylinder (1) in relation to the housing (2), which is carried out by means of three displacement sensors and a second order approximation (Equations (7) ff) yields the momentary minimum thickness h_{\min} and its lateral location β . A correlation study of h_{\min} and β versus the rotational speed shows a progressive increase of the minimum film thickness (Δh_{\min}) vs. the downstream movement of its lateral position ($\Delta \beta$) compared to the rigid case. In summary, elasticity causes the minimum film thickness to move towards the divergent part of the fluid film. The relation between Δh_{\min} and $\Delta \beta$ is displayed in Figure 9.

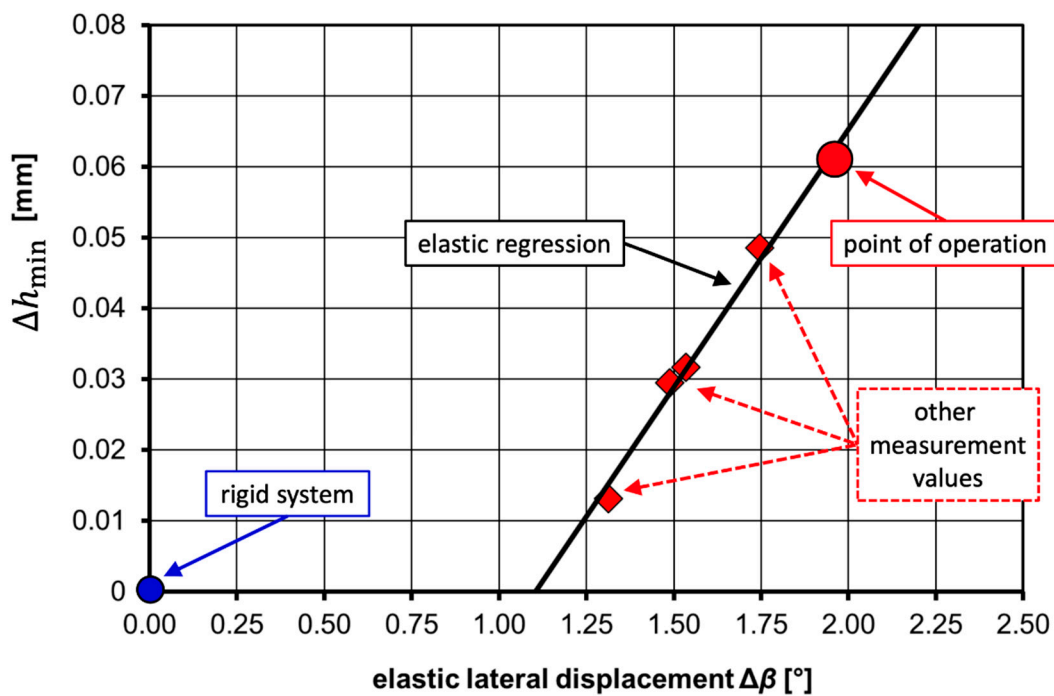


Figure 9. Elastic behavior of the Couette apparatus, rigid system vs. elastic system with increased film thickness Δh_{min} and lateral shift $\Delta\beta$.

The apparatus behaves like an ideal, rigid system when operated at very low speeds (< 0.1 1/s) or if it is filled with a low viscosity fluid, e.g., air instead of a paraffin. In both cases, the pressure that builds in an eccentric Couette flow is significantly less than 1 MPa does not result in any displacement of the components. However, when operated with the cavitating fluid (viscosity μ_0) at a rotational speed ω_1 a peak pressure of 227 kPa is generated and the center of the cylinder (1) is deflected, resulting in an increase in the film thickness of approximately 30%. This radial displacement combines with a downstream movement of the location of the minimum film thickness represented by the angle $\Delta\beta$ of nearly 2° , which is displayed in Figure 9. This lateral displacement appears to be insignificant, but when looking at the angular distance of the pressure extrema, which can be estimated by Equation (22) based on the journal bearing theory laid out by Hutter [33]

$$\Delta\varphi = 2 \cdot \arccos\left(\frac{3\varepsilon}{2 + \varepsilon^2}\right) \tag{22}$$

and according to the data listed in Table 1 the magnitude of the ratio becomes

$$\frac{\Delta\beta}{\Delta\varphi} = 0.0857. \tag{23}$$

Moreover, it is necessary to match the numerical model with the experiment and as described in Section 3, the model applies structured meshing which includes a strong geometric relation between the rotating cylinder (1) and the housing (2). Hence, the elastic displacement must be taken into consideration by assuming linear regression for Δh_{min} in the vicinity of the point of operation indicated in Figure 9 that equates to

$$\Delta h_{min} = 0.0806mm \cdot \left(\frac{\Delta\beta}{1.104^\circ} - 1\right). \tag{24}$$

Equation (24) is applied to the geometric relations, which are displayed by the schematic in Figure 2 to calculate the momentary position of the rotating cylinder (1) as a function the rotational angle

$$\Delta x_1 = e_1 \cdot \sin(\beta(\phi) + \Delta\beta) \Delta y_1 = -e_1 \cdot \cos(\beta(\phi) + \Delta\beta) \tag{25}$$

with

$$e_1 = e'_1(\phi) - \Delta h_{min} \tag{26}$$

and

$$e'_1(\phi) = E_0 \cdot \sqrt{1 + \lambda^2 - 2 \lambda \cos\phi}. \tag{27}$$

The validity of the elastic correction becomes clearly visible in Figure 10, which compares actual displacement values measured and computed data. For rigid conditions, the minimum film thickness h'_{min} is computed according to Equation (4). For real operational conditions when the cavity is filled with paraffin and the rotational speed is ω_1 , Figure 10 displays data for h_{min} according to Equation (6) in combination with

$$\beta_1 = \beta(\phi) + \Delta\beta. \tag{28}$$

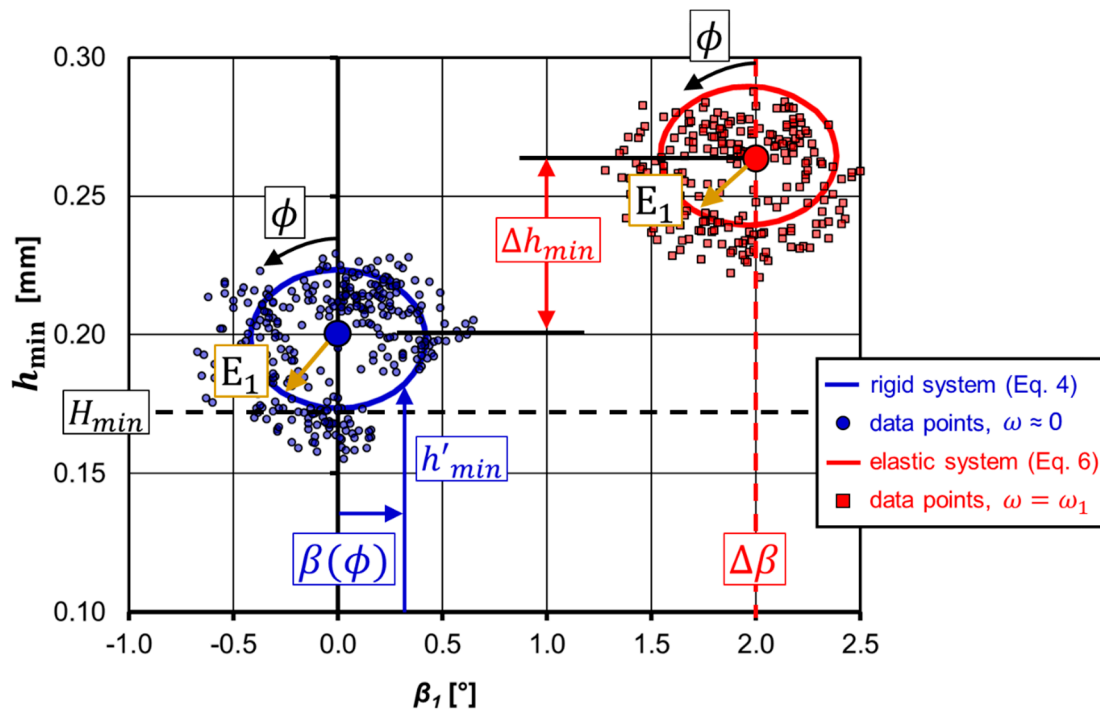


Figure 10. Elastic behavior of the Couette apparatus, rigid system vs. elastic system with measured displacement data and calculated minimum film thickness by means of the elastic correction.

According to [5], the definition of a small gap flow is met if the clearance is less than 0.3 mm and Figure 10 illustrates that the Couette apparatus complies with this definition, because in the vicinity of the minimum film thickness, the clearance is between 0.15–0.23 mm in the rigid case and 0.23–0.28 mm under real operation including the elastic deflection of the rotating cylinder.

7. Results

7.1. Steady Conditions

The formation of a large accumulation of vapor in the divergent section of a Couette flow with favorable conditions of eccentricity and Re is well documented in the community. A well cited reference is Jakobsson et al. [34] who presented experimental data. Cupillard et al. [35] applied a commercial CFD program whereas, [32] used open source software. More recently, Böhle [36] expanded the Reynolds model for flows across a permeable wall. However, it is necessary to apply a 3D-model based on Equation (12) that includes surface tension combined with an appropriate grid size to capture the true three-dimensional structure of the vapor bubbles in the divergent fluid film. Figure 11 represents the imaging area 1 as specified in Figure 3 and displays (a) the numerical result and (b) a photographic image illustrating the finger-like structure of the bubbles that are streamlined in the flow directed from left to right.

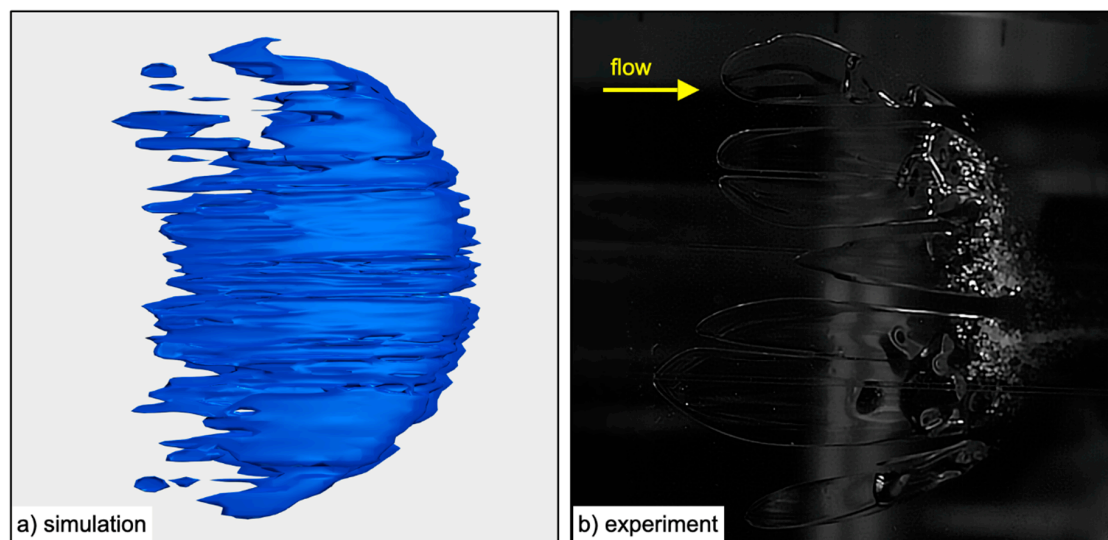


Figure 11. Steady cavitation zone in the divergent section of a fluid film, imaging area 1 according to Figure 3: (a) numerical results, iso-surface of 20% vapor volume fraction computed with a transient and three-dimensional two-phase model based on extended Navier–Stokes equations and 12 cells across the film, (b) high speed image of the flow inside the Couette apparatus (Figure 1) at $Re = 134$, $\Psi = 2.47\%$ and $\varepsilon = 94.4\%$.

The computation of the formation of vapor in the divergent section of the fluid film requires additionally to the modeling features mentioned above empirical constants such as the evaporation and the condensation coefficient as specified in Equations (16) and (17), respectively. These coefficients must be calibrated to the fluid under consideration. An important feature of the shape of the bubbles is the streamline structure that divides the vapor zone into finger-like elements, which is a result of the extension of the Navier–Stokes equations (Equation (12)) by a surface tension term. This term becomes important, if bubbles make contact with a solid wall and a contact angle between gaseous matter and liquid on the wall has to be considered. Another detail of the steady vapor zone in the divergent part of the fluid film is the local flow dynamic on the trailing edge of the bubbles (on the right side in each picture), where the film thickness is higher and the discontinuity surface is subject to a re-circulating flow in the wake of the bubbles. This can be observed in a movie much better than in still pictures. For this work, the excellent agreement between numerical and experimental results provides proof of a successful calibration that is henceforth applied to the transient changes of the flow caused by dynamic eccentricity and a second more rapid disturbance, which are addressed in the following section.

7.2. Transient Conditions

The set-up includes a co-axial alignment of the cylinder (1) between its centerline and its axis of rotation that causes a dynamic eccentricity, which results in a periodic variation of the film thickness synchronized with the rotational speed. According to our proposal [19] to address suction cavitation, a kinematic factor can be calculated taking the dynamic eccentricity and its derivative into Equation (29)

$$K = \left| \frac{\varepsilon'}{(1 - \varepsilon)^3} \right| \tag{29}$$

yielding

$$K = 9.7. \tag{30}$$

This value is low compared to journal bearing flows subject to material cavitation due to suction. However, K can be considered an amplification of the steady pressure and thus, local cavitation can occur which is displayed in the images in Figure 12.

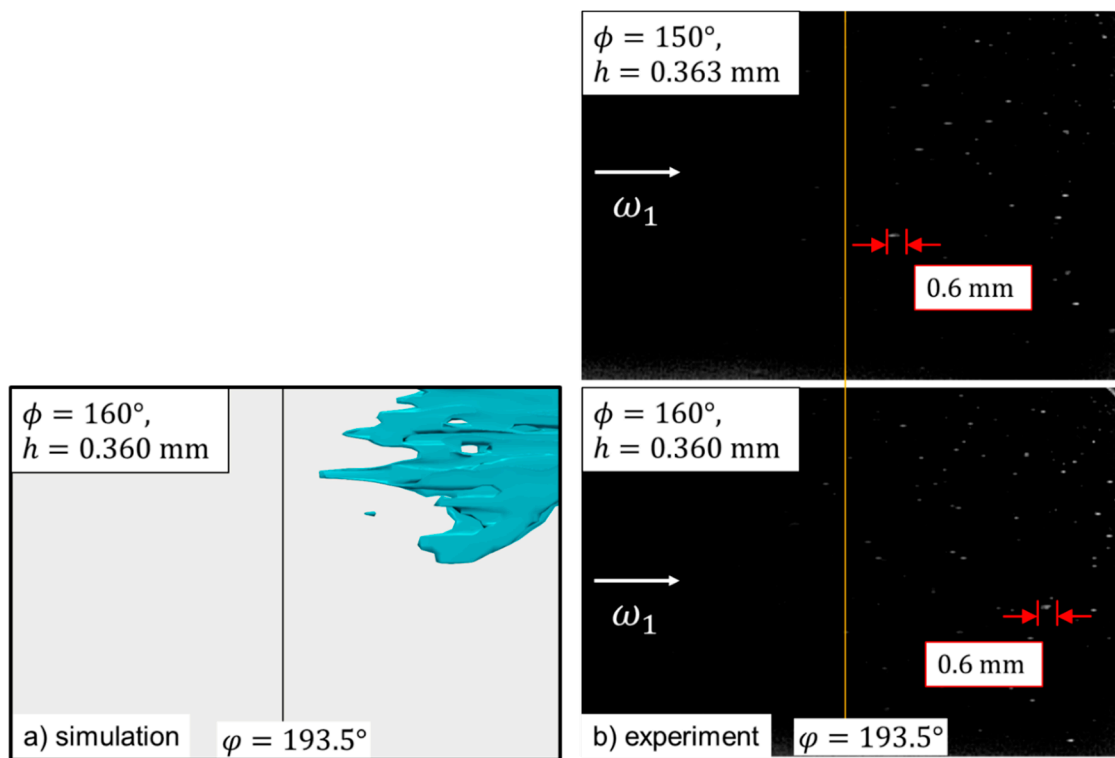


Figure 12. Dynamic cavitation zone in the divergent section of a fluid film, imaging area 2 according to Figure 3, rotational angle $\phi = 150^\circ$ – 160° : (a) numerical results showing the 10% volume fraction vapor computed with a transient and three-dimensional two-phase model based on extended Navier–Stokes equations and 12 cells across the film, (b) high speed image of the flow inside the Couette apparatus (Figure 1) at $Re = 134$, $\Psi = 2.47\%$ and $\varepsilon = 94.4\%$.

For the interpretation of the visualized data displayed in Figure 12, it is important to know the local film thickness which is calculated according to Sommerfeld’s theory [37] and incorporating both, the time scale expressed by the rotational angle and the elastic correction laid out in Section 6 leading to

$$h(\varphi, \phi) = H_0 + e_1(\phi, \Delta h_{min}) \cdot \cos(\varphi + \beta_1(\phi)). \tag{31}$$

Quantitatively, the data are combined in Figure 13 which presents the increase in vapor fraction evaluated for the section, as defined by Figure 3. The evaporation is triggered by the dynamic eccentricity which causes a decrease in local pressure beginning at $\phi = 45^\circ$. The increase in vapor fraction is rather a result of an increase in the number of bubbles detected by the image-processing tool than in individual bubble growth. Both distributions of normalized vapor fractions peak at an angular position of $\phi = 162^\circ$ which reflects the good agreement between experiment and simulation. A steep decrease representing the condensation of vapor succeeds the maximum over an equal angular segment, respectively. The duration and location of condensation are of fundamental interest pertaining a potential prediction of the region, which is subject to cavitation erosion. Thus, the results are promising. However, the comparison of the background level of the vapor fraction outside the peak region is not satisfactory due to unsteady experimental conditions resulting in a drift of the operation conditions, which are not entirely mirrored by the computation.

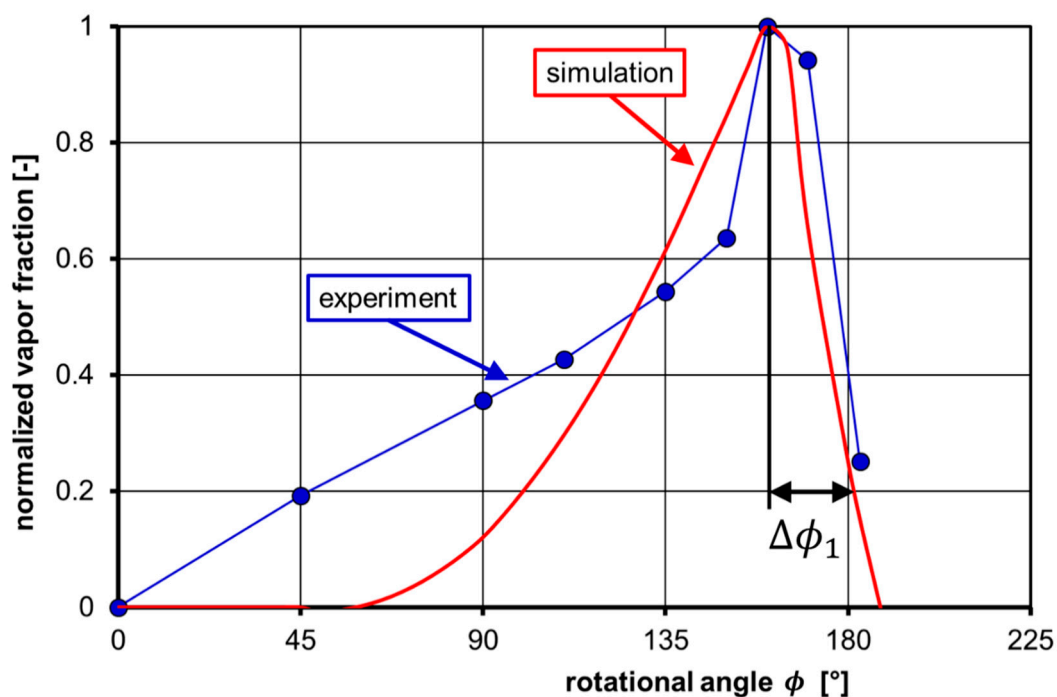


Figure 13. Gaseous fraction inside the dynamic cavitation zone in the divergent section of a fluid film vs. rotational angle ϕ : at $Re = 134$, $\Psi = 2.47\%$ and $\varepsilon = 94.4\%$.

The vapor curve should continue past 180° and decline symmetrically due the physics of the eccentricity governed by its harmonic equation (Equation (3)). Instead, the condensation appears much more rapidly. This rapid condensation is caused by a pressure wave resulting from an imperfection on the surface, a bulge located on the centerline of the rotating cylinder (1). The duration of this condensation becomes

$$\Delta t_1 = \frac{\Delta\phi_1}{\omega_1} = 15.3 \text{ ms} \tag{32}$$

with $\Delta\phi_1$ indicated in Figure 13. In relation to results presented by [3,4], it can be assumed that vapor cavitation is associated with the process. The position of the bulge is at the middle of the height of cylinder (1) and has a diameter of 24 mm and an elevation of 0.1 mm above the surface of the rotating cylinder. The magnitude of the pressure wave is this significant due to the fact that the bulge crossing the area of minimum film thickness blocks the highly reduced cross-section of the fluid film. Moreover, the transient nature of the condition is underlined when the bulge moves further downstream creating a suction pressure in its wake which, in turn, causes a second evaporation zone that is located inside

imaging area 2 that is specified in Figure 3. Based on the blocking ratio pertaining to the dimensions of the bulge, a corresponding kinematic parameter is estimated for this condition of $K = 1990$.

Hence, a second phase of local cavitation occurs at approx. 20° rotation later, which is displayed in Figure 14 for both, numerics and experiment taken at corresponding rotational angles. Again, the local film thickness is indicated next to the momentary rotation angle. During this second phase of cavitation, larger bubbles have formed. Whereas, the diameter of the earlier bubbles was about the same size as the film thickness, the current bubbles are larger and their radial axis exceeds the local film thickness. Hence, bubbles make contact with the walls and the contact angle between gaseous matter and liquid at the solid wall becomes important.

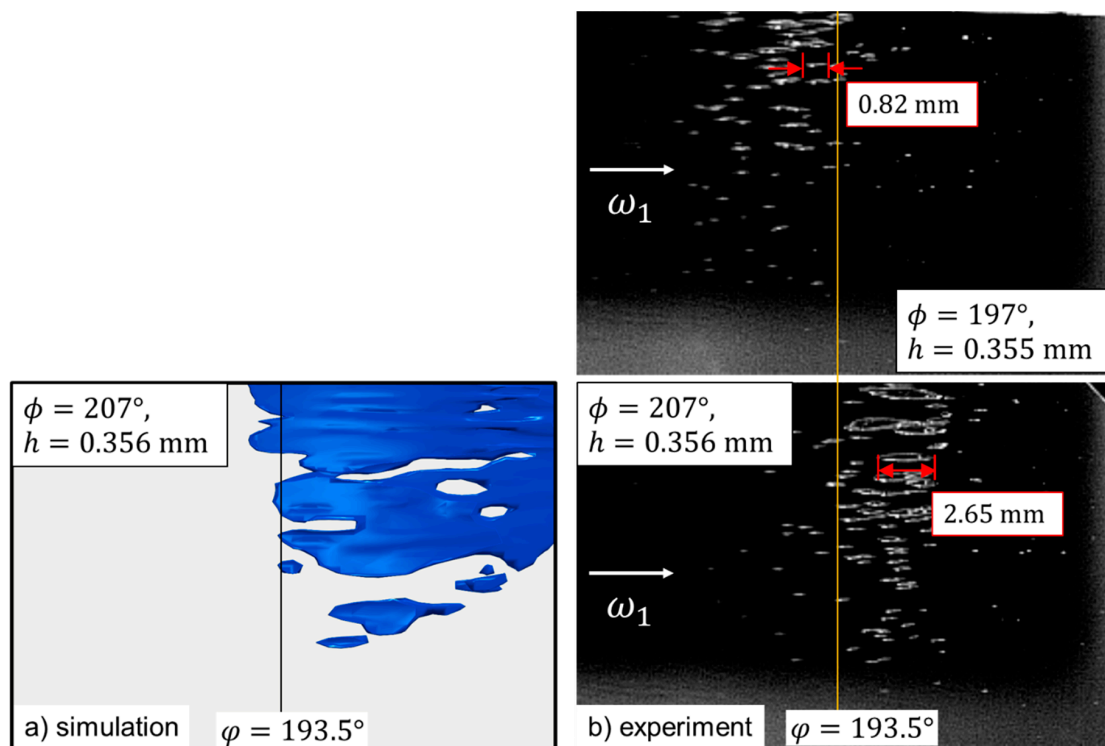


Figure 14. Dynamic cavitation zone in the divergent section of a fluid film, imaging area 2 according to Figure 3, rotational angle $\phi = 197^\circ$ – 207° : (a) numerical results showing the 30% volume fraction vapor computed with a transient and three-dimensional two-phase model based on extended Navier–Stokes equations and 12 cells across the film, (b) high speed image of the flow inside the Couette apparatus (Figure 1) at $Re = 134$, $\Psi = 2.47\%$ and $\varepsilon = 94.4\%$.

The second phase of cavitation is highly transient as it is presented in Figure 14 by the example of a bubble that has a length of 0.82 mm at $\phi = 197^\circ$ which increases to 2.65 mm at $\phi = 207^\circ$ yielding $\Delta\phi_2 = 10^\circ$. Taking into account that the clearance is nearly constant at $h = 0.356$ mm the bubble’s volume increases proportional with the visible cross-section, i.e.,

$$k = \left(\frac{2.65}{0.82}\right)^2 \approx 10 \tag{33}$$

in other words, the volume growth rate per time becomes

$$\dot{V}_B \approx 98 \frac{\text{mm}^3}{\text{s}} \tag{34}$$

and its duration according to Equation (32) is

$$\Delta t_2 = \frac{\Delta \phi_2}{\omega_1} = 7.5 \text{ ms} \quad (35)$$

It shall be pointed out that the numerical results display the 30% iso-surface of the vapor volume fraction, which underlines the substantial growth in vapor volume in just 7.5 ms. Again, this duration is substantially shorter than any reaction time documented for the case of gaseous cavitation. In summary, transient variations of the film thickness result in pressure gradients that, in turn, have an immense impact on cavitation. A sudden pressure increase might force condensation as shown in Figure 13 whereas, a sudden decrease will lead to strong production of vapor, as shown in Figure 14. Consequently, the assumption is substantiated that the subject of this work is vapor cavitation.

8. Discussion

This work presents simulations carried out with a transient, three-dimensional two-phase model that combines the volume-of-flow method with the Rayleigh–Plesset equation, an approach that is well established for the computation of cavitation, i.e., the generation and transportation of vapor bubbles inside a liquid flow. The special application is a small gap flow with a clearance of less than 0.3 mm. The numerical results are validated with experimental data that have been obtained with a Couette apparatus particularly designed for narrow gaps with a high (>90%) eccentricity. Another particularity of the experiment is the correction of the elasticity of the apparatus. A first-order correction is applied to the displacement of the rotating inner cylinder, which enables a better fitting of the numerical model to the experiment. Moreover, experiment and numerical models include transient changes of the film thickness, which affect the pressure distribution and the flow of the fluid film. Whereas, the numerical model applies the Schnerr–Sauer model to predict cavitation, the experiment uses a tailored fluid specifically designed to vaporize at the point of operation. A method that the authors have originally tested on the cavitating Taylor–Couette flow and, which they have herewith transferred to the eccentric Couette flow that is a model of the lubricant flow in journal bearings. This work presents experimental and numerical results of the bubble generation and its transportation in a Couette-type flow under the influence of shear and a strong pressure gradient which are typical for journal bearings or hydraulic seals. Under the impact of variations of the film thickness, the VoF method produces reliable results if bubble diameters are less than half the clearance between the walls. For larger bubbles, the wall contact becomes significant and the bubbles adopt an elliptical shape forced by the shear flow and under the influence of a strong pressure gradient. Moreover, transient changes of the pressure result in transient cavitation, which is captured by high-speed imaging providing material to evaluate transient, three-dimensional computations of a two-phase flow.

Future studies will aim at the investigation of transient conditions defining flow and vaporization of the fluid film combined with an expansion of the parameter range (see Figure 4) towards journal flows incorporated in a DoE approach, respectively. Additionally, the direct conformation of vapor cavitation is has not yet been presented and there remains a demand of future work. The transparent design of the Couette apparatus enables the application of optical methods such as Raman spectroscopy targeting vapor bubbles. As temperature and pressure are known, the Raman shifted spectrum is directly related to the gaseous matter that fills a bubble. However, optical analysis calls for a high operational effort and other readily available means should be considered, too. Gas analysis is a common technology in the automotive industry and the detection of hydro-carbons is reliable, which opens an avenue to prove that evaporated components of the paraffin-based cavitating fluid can be detected in a gas sample taken during the experiment.

Author Contributions: Conceptualization & methodology, P.R.; software, M.S.; validation, T.B., J.A., P.R.; formal analysis, P.R.; camera & optical resources, J.A.; experiments & data curation, T.B.; writing—original draft preparation, P.R.; writing—review and editing, P.R., J.A., T.B. and M.S.; visualization, M.S.; supervision & project administration, P.R.; funding acquisition, P.R. All authors have read and agreed to the published version of the manuscript.

Funding: This research received no external funding.

Acknowledgments: The authors wish to acknowledge the constant support of Wolfgang Viöl, Vice President of Research and Transfer at the HAWK Goettingen.

Conflicts of Interest: The authors declare that there is no conflict of interest.

Nomenclature

B	cylinder height, fluid film width
C_C	condensation coefficient
C_V	evaporation coefficient
E_0	static eccentricity
E_1	dynamic eccentricity
e_1	resulting eccentricity
e'_1	rigid eccentricity
e_{el}	elastic displacement
g	gravity constant
H_0	clearance between cylinder (1) and cavity (2)
H_{min}	absolute minimal fluid film thickness
h	local, transient film thickness
h_{min}	momentary minimal fluid film thickness
h'_{min}	rigid minimal fluid film thickness
Δh_{min}	elastic change of fluid film thickness
K	kinematic parameter
K_0	bulk modulus
k	constant
n	surface normal vector
\dot{m}^+	mass flow at evaporation
\dot{m}^-	mass flow at condensation
p	local pressure
p_0	reference pressure
p_{max}	maximum pressure
p_{min}	minimum pressure
p_v	vapor pressure
Δp	pressure difference
R_1	radius of inner cylinder
R_2	radius of cavity
R_B	radius of bubble
\dot{R}_B	bubble expansion velocity
t	time
u	fluid velocity
u_α	interface compression velocity
V_1	liquid volume
V_v	vapor volume
Δx_1	displacement of cylinder (1)
y	displacement reading
Δy_1	displacement of cylinder (1)

Greek Symbols

α	volume fraction
β	lateral displacement of minimum film thickness
β_1	resulting lateral displacement of minimum film thickness

$\Delta\beta$	elastic lateral displacement of minimum film thickness
δ	lateral spacing of displacement sensors
ε	relative eccentricity
ε_0	relative static eccentricity
ε_1	relative dynamic eccentricity
κ	compression exponent
λ	eccentricity ratio
μ_0	dynamic viscosity
ρ	local density
ρ_0	reference density
ρ_l	liquid density
ρ_v	vapor density
σ	surface tension
φ	Sommerfeld angle
ϕ	rotational angle
Ψ	normalized clearance
ω_1	rotational speed of inner cylinder

Mathematical Operators

$\vec{\nabla}$	nabla operator
sgn	signum function
Δ	difference

References

1. Borbe, P.C. Beitrag zur Werkstoffzerstörung durch Strömungskavitation in Kalten und Warmen Brauchwässern. Ph.D. Thesis, Universität Hannover, Hanover, Germany, 1968.
2. Braun, M.J.; Hannon, W.M. Cavitation formation and modelling for fluid film bearings: A review. *Proc. Inst. Mech. Eng. Part J J. Eng. Tribol.* **2010**, *224*, 839–863. [[CrossRef](#)]
3. Sun, D.C.; Brewe, D.E. *Two Reference Time Scales for Studying the Dynamic Cavitation of Liquid Films*; NASA Tech. Memo. 103673, AVSCOM Tech. Rep. 90-C-030; NASA: Washington, DC, USA, 1991.
4. Pendowski, D.; Pischinger, S. *Dynamic Oil Pressure in Connecting Rod Bearings and Their Influence on Innovative Cranktrain Technologies*; JSAE 20199283, SAE 2019-01-2333; SAE: Warrendale, PA, USA, 2019.
5. Xu, J.; Cheng, P.; Zhao, T. Gas–liquid two-phase flow regimes in rectangular channels with mini/micro gaps. *Int. J. Multiph. Flow* **1999**, *25*, 411–432. [[CrossRef](#)]
6. Tryggvason, G.; Dabiri, S.; Aboulhasanzadeh, B.; Lu, J. Multiscale considerations in direct numerical simulations of multiphase flows. *Phys. Fluids* **2013**, *25*, 031302. [[CrossRef](#)]
7. Braun, M.J.; Dzodzo, M. Three-Dimensional Flow and Pressure Patterns in a Hydrostatic Journal Bearing Pocket. *J. Tribol.* **1997**, *119*, 711–719. [[CrossRef](#)]
8. Schmidt, M. Untersuchung der dreidimensionalen Strömung in Radialgleitlagern. Ph.D. Thesis, Brandenburgische Technische Universität Cottbus-Senftenberg, Cottbus, Germany, 2016.
9. Nobis, M. Experimentelle Untersuchung der Spaltströmung in Einem Modell Eines Kurbelwellenhauptlagers. Ph.D. Thesis, BTU Cottbus-Senftenberg, Cottbus, Germany, 2017.
10. Gläser, H. *Schäden an Gleit- und Wälzlagerungen*; Verlag Technik: Berlin, Germany, 1990.
11. DIN ISO 7146-1. *Erscheinungsbild und Charakterisierung von Schäden an Ölgeschmierten Metallischen Gleitlagern*; Deutsches Institut für Normung E.V., Beuth Verlag: Berlin, Germany, 2008.
12. Garner, D.R.; James, R.D.; Warriner, J.F. Cavitation Erosion Damage in Engine Bearings: Theory and Practice. *J. Eng. Power* **1980**, *102*, 847–857. [[CrossRef](#)]
13. Engel, U. Schäden an Gleitlagern in Kolbenmaschinen. In *Schäden an Geschmierten Maschinenelementen*; Bartz, W., Auflage, Z., Eds.; Expert-Verlag: Renningen, Germany, 1992.
14. Almqvist, T.; Larsson, R. Some Remarks on the Validity of Reynolds Equation in the Modeling of Lubricant Film Flows on the Surface Roughness Scale. *J. Tribol.* **2004**, *126*, 703–710. [[CrossRef](#)]
15. Sharma, S.L.; Ishii, M.; Hibiki, T.; Schlegel, J.P.; Liu, Y.; Buchanan, J.R. Beyond bubbly two-phase flow investigation using a CFD three-field two-fluid model. *Int. J. Multiph. Flow* **2019**, *113*, 1–15. [[CrossRef](#)]

16. DiPrima, R.C. A Note on the Stability of Flow in Loaded Journal Bearings. *ASLE Trans.* **1963**, *6*, 249–253. [[CrossRef](#)]
17. Eagles, P.; Stuart, J.T.; DiPrima, R.C. The effects of eccentricity on torque and load in Taylor-vortex flow. *J. Fluid Mech.* **1978**, *87*, 209–231. [[CrossRef](#)]
18. Kahlert, W. Der Einfluß der Trägheitskräfte bei der Hydrodynamischen Schmiermitteltheorie. *Ing. Arch.* **1946**, *16*, 321–342. [[CrossRef](#)]
19. Reinke, P.; Schmidt, M.; Beckmann, T. *Advanced Model Experiment for the Research of Journal Bearings with Cavitation*; SAE Technical Paper Series; SAE International: Warrendale, PA, USA, 2019.
20. Reinke, P.; Schmidt, M.; Beckmann, T. The cavitating Taylor-Couette flow. *Phys. Fluids* **2018**, *30*, 104101. [[CrossRef](#)]
21. Beckmann, T.; Reinke, P.; Schmidt, M. Proceedings in Fluiddesign. *PAMM* **2019**, *19*. [[CrossRef](#)]
22. Watter, H. *Hydraulik und Pneumatik*; Springer: Berlin/Heidelberg, Germany, 2007; ISBN 978-3-8348-9416-8.
23. Schmidt, M.; Reinke, P.; Beckmann, T. Numerical simulation of suction cavitation in hydrodynamic journal bearings. *PAMM* **2019**, *19*. [[CrossRef](#)]
24. OPENCFD. *OpenFOAM-The Open Source CFD Toolbox-User Guide*; Version v1806; OpenCFD Limited: Berkshire, UK, 2018.
25. Schmidt, M.; Reinke, P.; Rabanizada, A.; Umbach, S.; Rienäcker, A.; Branciforti, D.; Philipp, U.; Bargende, M.; Preuß, A.-C.; Pryymak, K.; et al. Numerical Study of the Three-Dimensional Oil Flow Inside a Wrist Pin Journal. *Tribol. Trans.* **2020**, 1–10. [[CrossRef](#)]
26. Kistner, B. Modellierung und Numerische Simulation der Nachlaufstruktur von Turbomaschinen am Beispiel einer Axialturbinenstufe. Ph.D. Thesis, University Darmstadt, Darmstadt, Germany, 1999.
27. Jasak, H.; Tukovic, Z. Dynamic mesh handling in OpenFOAM applied to fluid-structure interactions simulation. In Proceedings of the V European Conference on Computational Fluid Dynamics ECCOMAS CFD, Lisbon, Portugal, 14–17 June 2010.
28. Ferziger, J.H.; Perić, M. *Numerische Strömungsmechanik*; Springer: Berlin/Heidelberg, Germany, 2008; ISBN 978-3-540-67586-0.
29. Sauer, J. Instationär Kavitierende Strömungen—Ein Neues Modell, Basierend auf Front Capturing (VoF) und Blasendynamik. Ph.D. Thesis, Universität Karlsruhe, Karlsruhe, Germany, 2000.
30. Schnerr, G.H.; Sauer, J. Physical and numerical modelling of unsteady cavitation dynamics. In Proceedings of the 4th International Conference on Multiphase Flow, New Orleans, LA, USA, 27 May–1 June 2001.
31. Kumar, A.; Ghobadian, A.; Nouri, J.M. Assessment of Cavitation Models for Compressible Flows inside a Nozzle. *Fluids* **2020**, *5*, 134. [[CrossRef](#)]
32. Riedel, M.; Schmidt, M.; Reinke, P.; Nobis, M.; Redlich, M. Application of computational fluid dynamics on cavitation in journal bearings. *EPJ Web Conf.* **2014**, *67*, 2099. [[CrossRef](#)]
33. Hutter, K. *Fluid- and Thermodynamik—2. Aufl.*; Springer: Berlin/Heidelberg, Germany, 2003; ISBN 3-540-43734-7.
34. Jakobsson, B.; Floberg, L. The finite journal bearing, considering vaporization. *Trans. Chalmers Univ. Technol.* **1957**, *190*, 6–116.
35. Cupillard, S.; Glavatskih, S.; Cervantes, M.J. Computational fluid dynamics analysis of a journal bearing with surface texturing. *Proc. Inst. Mech. Eng. Part J J. Eng. Tribol.* **2008**, *222*, 97–107. [[CrossRef](#)]
36. Böhle, M. Numerical Investigation of the Flow in Hydrostatic Journal Bearings with Porous Material. In Proceedings of the Fluids Engineering Division Summer Meeting, Montreal, QC, Canada, 15–19 July 2018.
37. Sommerfeld, A. Zur hydrodynamischen Theorie der Schmiermittelreibung. *ZAMM* **1904**, *40*, 97–155.

Publisher’s Note: MDPI stays neutral with regard to jurisdictional claims in published maps and institutional affiliations.



© 2020 by the authors. Licensee MDPI, Basel, Switzerland. This article is an open access article distributed under the terms and conditions of the Creative Commons Attribution (CC BY) license (<http://creativecommons.org/licenses/by/4.0/>).